PIC simulation of a thermal anisotropy-driven Weibel instability in a circular rarefaction wave

PIC simulation of a thermal anisotropy-driven Weibel instability in a circular rarefaction wave

M E Dieckmann[1,6], **G Sarri**[1], **G C Murphy**[2], **A Bret**[3],
L Romagnani[4], **I Kourakis**[1], **M Borghesi**[1], **A Ynnerman**[5]
and L O'C Drury[2]

[1] Centre for Plasma Physics, The Queen's University of Belfast,
Belfast BT7 1NN, UK
[2] Dublin Institute for Advanced Studies, 31 Fitzwilliam Place, Dublin 2, Ireland
[3] ETSI Industriales, Universidad de Castilla-La Mancha, 13071 Ciudad Real,
Spain and Instituto de Investigaciones Energticas y Aplicaciones Industriales,
Campus Universitario de Ciudad Real, 13071 Ciudad Real, Spain
[4] LULI, Ecole Polytechnique, CNRS, CEA, UPMC, 91128 Palaiseau, France
[5] MIT, Department of Science and Technology (ITN), Linköping University,
SE-60174 Norrkoping, Sweden
E-mail: Mark.E.Dieckmann@itn.lie.se

Abstract. The expansion of an initially unmagnetized planar rarefaction wave has recently been shown to trigger a thermal anisotropy-driven Weibel instability (TAWI), which can generate magnetic fields from noise levels. It is examined here whether the TAWI can also grow in a curved rarefaction wave. The expansion of an initially unmagnetized circular plasma cloud, which consists of protons and hot electrons, into a vacuum is modelled for this purpose with a two-dimensional particle-in-cell (PIC) simulation. It is shown that the momentum transfer from the electrons to the radially accelerating protons can indeed trigger a TAWI. Radial current channels form and the aperiodic growth of a magnetowave is observed, which has a magnetic field that is oriented orthogonal to the simulation plane. The induced electric field implies that the electron density gradient is no longer parallel to the electric field. Evidence is presented here that this electric field modification triggers a second magnetic instability, which results in a rotational low-frequency magnetowave. The relevance of the TAWI is discussed for the growth of small-scale magnetic fields in astrophysical

---

[6] Author to whom any correspondence should be addressed.

IOP Institute of Physics **Φ** DEUTSCHE PHYSIKALISCHE GESELLSCHAFT

environments, which are needed to explain the electromagnetic emissions by astrophysical jets. It is outlined how this instability could be examined experimentally.

S Online supplementary data available from stacks.iop.org/NJP/14/023007/mmedia

Contents

1. Introduction

Energetic electromagnetic radiation is emitted by a wide range of astrophysical objects, such as supernova remnants (SNRs) [1], microquasars [2] and gamma-ray bursts (GRBs) [3]. This radiation is at least partially attributed to the synchrotron- or synchrotron jitter emissions [4] of ultra-relativistic electrons, which gyrate in strong magnetic fields. Such extreme conditions do not exist in the interstellar medium, and probably not in astrophysical jets or in SNR blast shells, if their plasma is in a steady state. Efficient electron acceleration and magnetic field amplification mechanisms must be at work and they are driven primarily by collisionless plasma shocks [5].

Through their interaction with the electromagnetic fields in the shock transition layer, the electrons may gain enough energy to be injected into the diffusive shock acceleration process [6]. The latter is probably capable of accelerating charged particles to the highest observed cosmic ray energies and it should supply a population of highly relativistic electrons. The apparent magnetization of SNR shocks [7] is attributed to cosmic ray-driven instabilities, which can operate on large scales [8]. Filamentation instabilities of counterstreaming beams of charged particles are thought to be the origin of the micro-scale magnetic fields, in particular of those in GRB jets [9, 10], although the lifetimes of these fields may be too short [11, 12].

Filamentation or beam-Weibel instabilities develop in an initially spatially uniform system of two counterstreaming particle beams. Typically, one examines this instability in the reference frame, in which the net charge and current vanish. The beams consist of electrons and ions and may contain a sizeable fraction of positrons in GRB jets. The filamentation instability transforms the spatially uniform beams into a system of spatially separated current flux tubes, which are enwrapped and separated by electromagnetic fields [13–17]. Observations of the filamentation instability in laboratory settings and the resulting electromagnetic radiation exist [18] and they are likely to occur close to shocks [13] in astrophysical settings.

The Weibel instability [19] is another magnetic instability. It is driven by a thermal anisotropy of a single electron species. Weibel considered in his original work a spatially uniform bi-Maxwellian electron velocity distribution. The electrons were cooler along one direction than along the other two. The Weibel instability gives rise to the aperiodic growth of magnetowaves with a wavevector that is parallel to the cool direction [20] and with wavelengths that are comparable to an electron skin depth. The Weibel instability has been widely examined in the past, both analytically and numerically [21–30]. Its importance for the generation of magnetic fields in jet outflows and on a cosmological scale has been pointed out [31]. It has, however, previously been unclear how a strong thermal anisotropy could form and survive over spatial scales that exceed the wavelength of the modes, which are destabilized by the Weibel instability in its original form [19].

Such a process has recently been identified [32]. A plasma density gradient together with the high electron mobility gives rise to an ambipolar electrostatic field, which confines the electrons and accelerates the ions. The electric field vector is antiparallel to the density gradient. The ion acceleration launches a rarefaction wave [33–38]. The electrons, which move from the dense plasma to the front of the rarefaction wave, are slowed down and reflected inelastically by the electric field of the expanding wave, through which they provide the energy for the ion acceleration. The modulus of the electron momentum along the density gradient is reduced by these processes, while both orthogonal momentum components are unchanged. The thermal anisotropy can give rise to the Weibel instability. In what follows, we refer to it as the thermal anisotropy-driven Weibel instability (TAWI). Particle-in-cell (PIC) simulations [32] have shown that the TAWI can magnetize a planar plasma cloud that expands into a vacuum. A shock develops if the rarefaction wave expands into a dilute ambient medium. The TAWI is suppressed if a shock limits the extent of the rarefaction wave to a length that is shorter than the wavelength of its modes [37, 38].

This process, which requires ion density gradients and hot electrons, can be important for energetic astrophysical plasma. The internal shock model for the prompt GRB emissions assumes that the jet consists of plasma clouds with varying densities and mildly relativistic relative speeds [3]. We can also assume that the ion density close to SNR shocks will not be spatially uniform. The bulk electrons in the GRB jets are thought to be relativistically hot and the bulk electrons close to SNR shocks have keV temperatures. The magnetic energy generated by the TAWI can reach a sizeable fraction of the electron thermal energy, which could result in strong magnetic fields.

The TAWI has previously been examined numerically in a two-dimensional planar geometry. A plasma slab is centered in these studies in the simulation box and confined by two parallel boundaries, across which the density jumps from the constant high density within the slab to a low density or a vacuum outside of it. The plasma density is constant along the second simulation direction and the boundary conditions are periodic. The rarefaction waves launched at both boundaries move in opposite directions, causing an expansion of the slab plasma. The density gradients of both rarefaction waves are antiparallel. An electron can cross the slab many times and its momentum component along the density gradients remains decoupled from both orthogonal ones. Multiple electron reflections, which reduce only the electron momentum component along the plasma density gradient, result in an increasingly strong thermal anisotropy, which may exaggerate the strength of the TAWI.

We examine here with a particle-in-cell (PIC) simulation the expansion of an initially unmagnetized circular plasma cloud. The electron momentum cannot in this case be subdivided

into a component that is always parallel to the density gradient and into two components orthogonal to it, unless the electron moves exactly in the radial direction. This case is unlikely. Consecutive electron reflections by the electric field of the rarefaction wave will diminish different momentum components and the anisotropy between the temperature in the radial and azimuthal directions is not boosted by multiple reflections. The purpose of our simulation study is to assess if the slowdown of the electrons in the sheath potential alone is still strong enough to trigger the TAWI.

Our results are as follows. The ambipolar electric field accelerates the protons in the simulations to a few per cent of c. A TAWI develops within the density gradient of the rarefaction wave. This instability is similar to that observed in [32]. It drives radial current channels, which yield the growth of a transverse magnetic (TM) field component. The growth of the TM wave is followed by that of a secondary transverse electric (TE) magnetowave. The rotational polarization of this TE wave is concluded from the simultaneous presence of in-plane magnetic vortices and out-of-plane magnetic fields that interfere with those driven by the TAWI. The combined magnetic field of both waves breaks the circular symmetry of the rarefaction wave and scatters rapidly the electrons within, thereby reducing their thermal anisotropy. The instability saturates in our simulation when the total magnetic energy density is about 1% of the electron thermal energy.

The TE and TM magnetowaves develop in the same radial interval, which suggests their connection. We propose that the superposition of the electric field, which is induced by the magnetic field of the TAWI, with the radial electric field of the rarefaction wave triggers the growth of the TE wave by the misalignment of the plasma density gradient and the electric field vector. Such a system is unstable [39, 40] and results in an instability similar to the thermoelectric.

The structure of this paper is as follows. Section 2 describes the PIC simulation code and the initial conditions. Our results are presented in section 3. Section 4 summarizes our findings and discusses how these could be verified experimentally.

2. The simulation code and the initial conditions

The 2D3V (resolves two spatial and three momentum dimensions) PIC simulation code we employ here is based on the virtual particle-mesh numerical scheme [41]. Faraday's and Ampère's laws

$$\nabla \times \mathbf{E} = -\frac{\partial \mathbf{B}}{\partial t}, \tag{1}$$

$$\nabla \times \mathbf{B} = \mu_0 \mathbf{J} + \mu_0 \epsilon_0 \frac{\partial \mathbf{E}}{\partial t} \tag{2}$$

are solved on a grid and evolve the electromagnetic fields in time, while $\nabla \cdot \mathbf{E} = \rho/\epsilon_0$ and $\nabla \cdot \mathbf{B} = 0$ are fulfilled as constraints. The code solves all three field components as a function of $\mathbf{x} = (x, y)$. The relativistic force equation

$$\frac{\mathrm{d}\mathbf{p}_i}{\mathrm{d}t} = q_j (\mathbf{E}[\mathbf{x}_i] + \mathbf{v}_i \times \mathbf{B}[\mathbf{x}_i]) \tag{3}$$

is used to update the momentum of the ith computational particle (CP) of species j, with charge q_j and mass m_j, that is located at the position $\mathbf{x}_i$. The electric $\mathbf{E}$ and magnetic $\mathbf{B}$ fields are
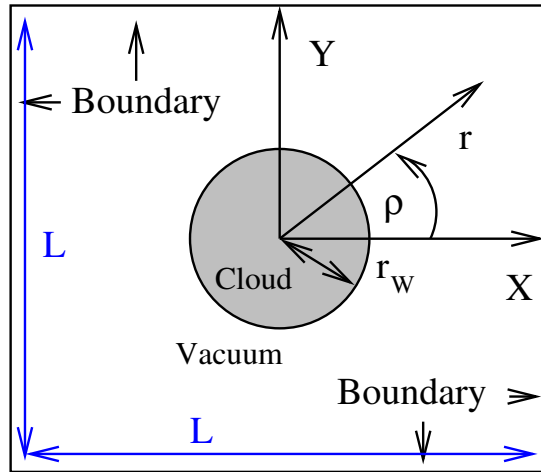
Figure 1. The 2D simulation plane covers the interval $-L/2 < x, y < L/2$. A circular plasma cloud has its center at $x, y = 0$ and the radius $r_W = L/5.4$. It is filled with electrons and protons with the density n_0. The boundary conditions are periodic for the fields and for the particles. We will in some cases exploit the circular symmetry and use the circular coordinates (r, ρ) instead of (x, y).

connected with the CPs as follows. The micro-current of each CP is interpolated to the grid. The sum of the interpolated micro-currents of all CPs gives the macroscopic current **J**, which is used to update the electromagnetic fields through equation (2). The new fields are interpolated back to the positions of the individual CPs to update their momentum in time through equation (3). The position of each CP is updated with $d\mathbf{x}_i/dt = (v_{i,x}, v_{i,y})$. A detailed review of the PIC method is given elsewhere [42].

The plasma cloud with radius r_W is surrounded by vacuum and consists of electrons with the number density n_0 and protons with the same density, which are initially distributed uniformly across the cloud. Figure 1 illustrates the setup. The electron's relativistic Maxwellian velocity distribution has a temperature of 32 keV or a thermal speed $v_e = c/4$. The proton thermal speed in both simulations is $v_p = 3.1 \times 10^4 \, \mathrm{ms}^{-1}$ and corresponds to a thermal energy of 10 eV. The mean speeds of the electrons and of the protons vanish initially. The electrons and protons are approximated each by $\approx$2500 CPs per cell. The electron mass is m_e and the proton mass $m_p = 1836 m_e$. The initial electron skin depth $\lambda_e = c/\omega_p$ is and the electron plasma frequency is $\omega_p = (n_0 e^2/m_e \epsilon_0)^{1/2}$. Time is expressed in units of ω_p^{-1}. The time step is $\Delta_t = 0.022$. The simulation time is $T_F = 880$. The cloud radius $r_W = 14.2\lambda_e$. An electron with the thermal speed v_e will cross the cloud diameter $2r_W$ about eight times during $t = T_F$, resulting in multiple bounces at the electrostatic sheath field. The simulation box with periodic boundary conditions in all directions uses 1700×1700 cells for a square domain with the side length $L = 75.5\lambda_e$.

3. The simulation results

We examine the plasma phase space distributions and the electromagnetic field distributions, the loss of electron thermal energy to the protons and the thermal anisotropy. We consider in
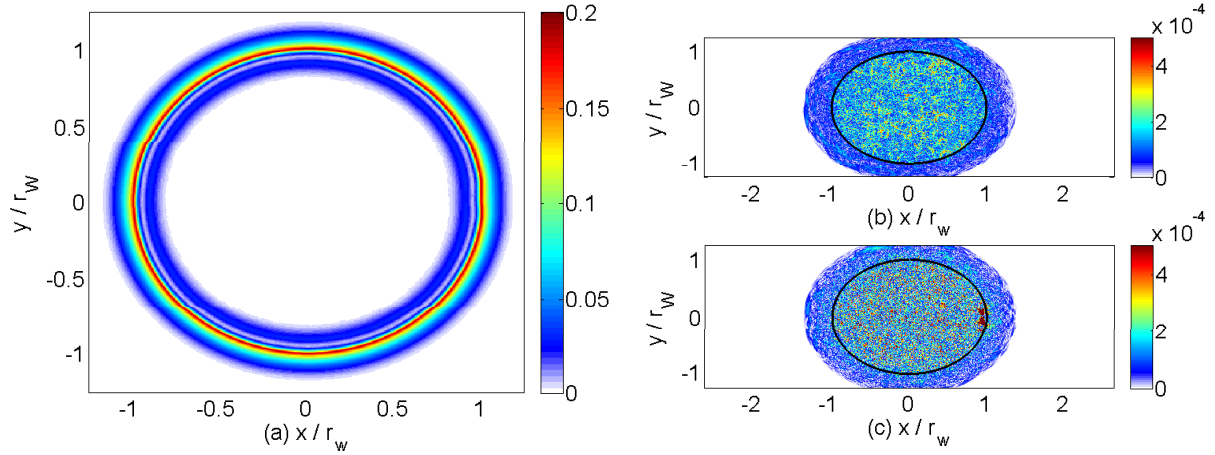
Figure 2. The field distributions at time T_1: (a) the modulus of the in-plane electric field E_p, (b) the in-plane magnetic field B_p and (c) the orthogonal field $|B_z|$. A strong electric field points radially outwards and outlines the cloud's perimeter. The magnetic fields are at noise levels. Overplotted is a black circle with $r = r_W$.

more detail the simulation times $T_1 = 5.5$, $T_2 = 550$ and $T_3 = 750$. This section concludes with a discussion of the time evolution of the plasma quantities and effects due to the periodic boundary conditions.

We transform the distributions from a representation in (x, y)-space into the one in (r, ρ)-space, where $r = 0$ is the center of the cloud and of the simulation box. We exploit the approximate circular symmetry and average these quantities over the azimuth angle ρ. This average will become less accurate at late times, when **B** breaks this symmetry. The electron number density $\tilde{n}_e(r) = \int n_e(r, \rho) r \, d\rho$. The phase space densities $f_{e,p}(r, \rho, v_r, v_\rho, v_z)$ are integrated as $\tilde{f}_{e,p}(r, v_r) = r^{-1} \int f_{e,p} r \, d\rho \, dv_\rho \, dv_z$, where e and p stand for electrons and protons. The phase space densities at all times are normalized to the maximum of the respective distribution at $t = 0$. The azimuthally averaged radial thermal energy $K_r(r) = K_0^{-1} \int_\rho r \, d\rho \int f_e v_r^2 \, d\mathbf{v}$ and azimuthal thermal energy $K_\rho(r) = K_0^{-1} \int r \, d\rho \int f_e v_\rho^2 \, d\mathbf{v}$ define the thermal anisotropy $A(r) = K_r(r)/K_\rho(r)$. The initial electron thermal energy per degree of freedom is K_0. The in-plane electric field $E_p = |E_x + iE_y|$ and the orthogonal E_z field are expressed in units of $\omega_p c m_e/e$, while the magnetic field components $B_p = |B_x + iB_y|$ and B_z are expressed in units of $\omega_p m_e/e$. The fields are azimuthally averaged as $\langle F^2 \rangle = (2\pi r)^{-1} \int_\rho F^2 r \, d\rho$, where F serves as a place holder for E_p, E_z, B_p and B_z.

3.1. Early time T1: proton acceleration

Their mobility implies that some electrons can escape from the cloud and build up a negatively charged sheath outside of the now positively charged cloud. An ambipolar electrostatic field develops that points along the surface normal. Its modulus is displayed in figure 2 for the time T_1. The electric field outlines the cloud radius and has a thickness comparable to λ_e. The magnetic B_p and B_z components show noise that is strongest for $r < r_W$ and weaker in the rarefaction wave. The noise originates from statistical fluctuations of the current density.
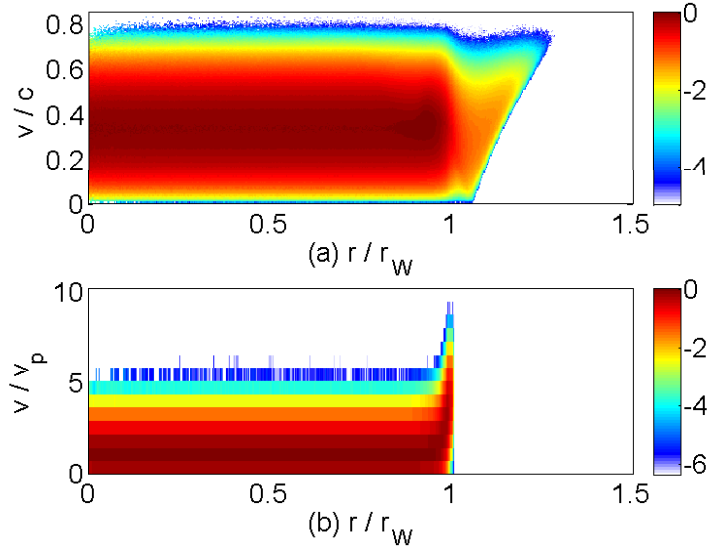
Figure 3. The azimuthally averaged radial phase space density at the time T_1 normalized to its initial value: (a) and (b) $\tilde{f}_e$ and $\tilde{f}_p$, respectively. The color scale is 10-logarithmic and r_W is the initial cloud radius.

The initial plasma evolution is dominated by the electrostatic fields because their amplitude is much larger than the amplitude of the magnetic fields and because the latter are incoherent.

The protons are accelerated radially outwards by the electric field, which confines at the same time the electrons. This is confirmed by figure 3. The electrons lose speed in the radial direction and their density decreases drastically as they cross the strong in-plane electric field E_p at $r = r_W$. This field is not strong enough to hold back all electrons and some escape into the vacuum. The fastest electrons have expanded to a radius $r \approx 1.3 r_W$, while the proton expansion is still negligible. The protons with $r \approx r_W$ are accelerated by E_p and some reach already at the time T_1 a peak speed that exceeds their initial thermal speed v_p by an order of magnitude. The protons with $r < r_W$ still show their initial velocity distribution. Their low thermal speed implies that they could not yet interact with the surface electric field.

3.2. Intermediate time T2: the thermal anisotropy-driven Weibel instability

Figure 4 shows the particle distributions at time T_2. The protons have been accelerated by the ambipolar electric field to about $200 v_p$ or to 2% of the speed of light c. The protons form a narrow beam with a speed that grows approximately linearly with r for $r > 0.7 r_W$ and a density that decreases with increasing radius. This high speed has been reached by the protons, because there is no shock that limits their acceleration. A shock would form if the rarefaction wave were to expand into an ambient plasma. The electron distribution has been altered significantly at this time. The peak speed of the electron's bulk population in the cloud's core, which has shrunk to $r < 0.7 r_W$ at this time, has been decreased compared to that in figure 3(a), which is indicative of an energy loss. This energy loss can be attributed to the electron's inelastic reflection by the ambipolar electric field of the expanding rarefaction wave. The electrons fill up the entire simulation box, although their phase space density close to the boundary is four orders of magnitude less than the peak density within $r < 0.7 r_W$.
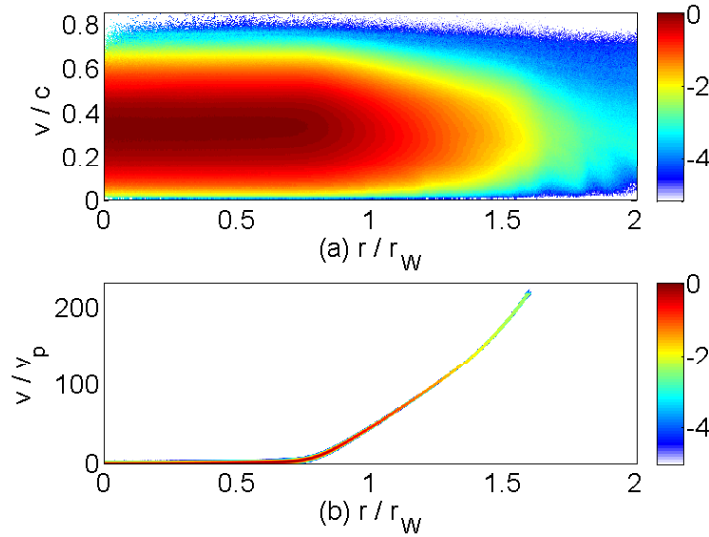
Figure 4. The azimuthally averaged radial phase space density at the time T_2 normalized to its initial value: (a) and (b) $\tilde{f}_e$ and $\tilde{f}_p$, respectively. The color scale is 10-logarithmic and r_W is the initial cloud radius.
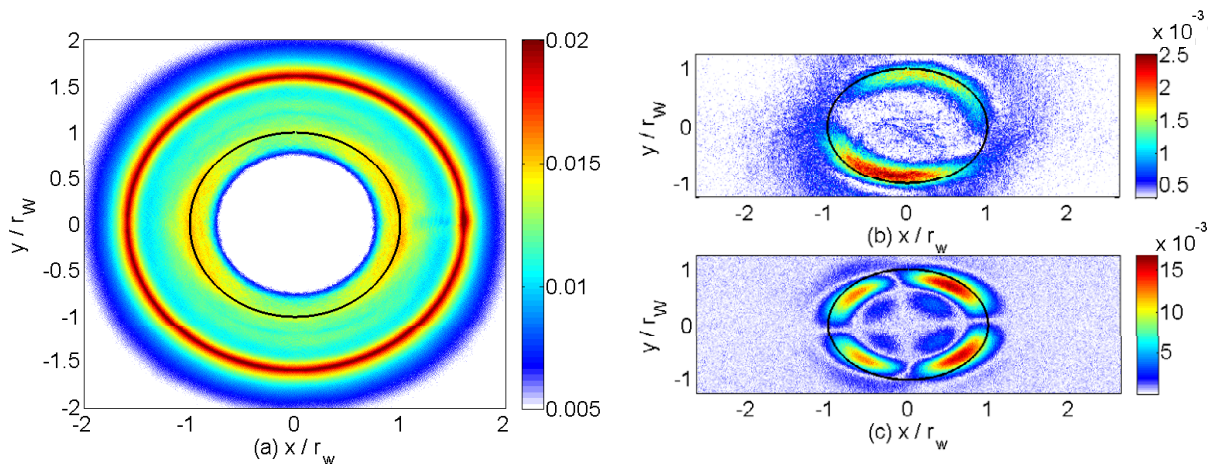

Figure 5. The field distributions at $t = T_2$: (a) the modulus of the in-plane electric field E_p and (b) that of the in-plane magnetic field B_p; (c) the modulus $|B_z|$. The black circles with radius r_W outline the initial cloud perimeter.

The erosion of the cloud implies that the initial distribution of E_p in figure 2(a) could not have been upheld. This is confirmed by figure 5, which shows the E_p, B_p and the modulus of B_z at time T_2. The electric field maximum is located at $r \approx 1.6 r_W$, which is at the tip of the expanding protons in figure 4(b). The electric field distribution expands to lower r. It thus continues to accelerate the protons and sustains the increase of the proton mean speed with the radius. The electric fields at $r \approx r_W$ are a consequence of the plasma density gradient in this interval and of the higher electron mobility, which implies a space charge. Figure 5(a) reveals that the electric field in the interval $r \approx r_W$ does not show an exact circular symmetry. The amplitude is a function of ρ.
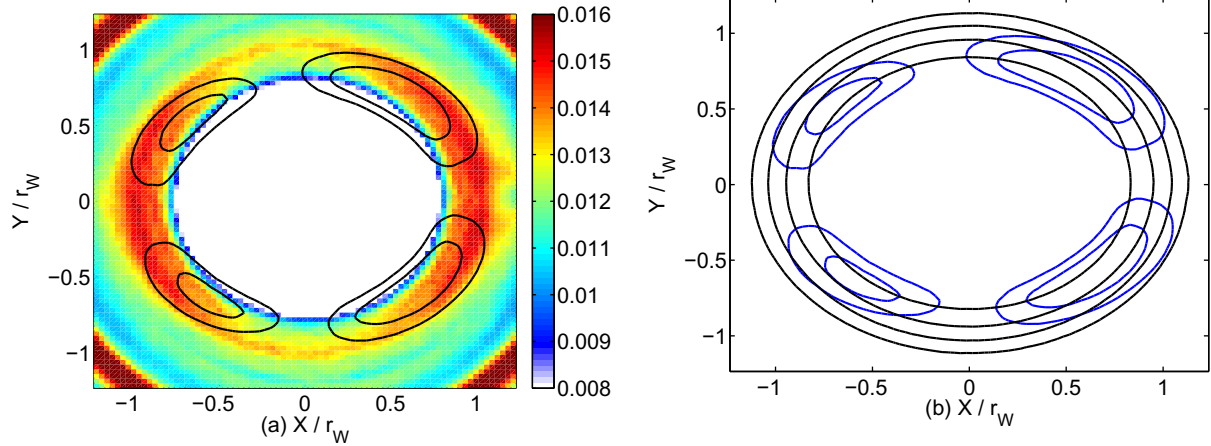
Figure 6. Panel (a) shows the modulus of the in-plane electric field $E_p(x, y)$. The contour lines correspond to the values $-0.01, -0.005, 0.005$ and 0.01 of the B_z field. The B_z field has maxima in the upper right and the lower left quadrant and minima in the other two quadrants. Panel (b) compares the same contour lines of B_z with the contour lines $2.7, 2.9, 3.1$ and 3.3 of the 10-logarithmic electron number density. The density increases with decreasing radius. The number density is expressed in CPs per cell and $\log_{10} n_0 = 3.4$.

This break of the circular symmetry and its origin become evident in figure 6, which shows the amplitude modulus of E_p and the electron density distribution in the relevant spatial interval and compares both quantities to B_z. The amplitude of the azimuthal oscillation of E_p at $r \approx r_W$ is about 10% of the mean value. Figure 6(a) suggests a correlation of E_p with B_z for two reasons. Firstly, the azimuthal oscillation of E_p and the strong B_z are observed at approximately the same radius. Secondly, the E_p field shows two amplitude minima and two maxima, which are shifted by 45° relative to those of B_z. We find one maximum of E_p at $x \approx r_W$ and $y \approx 0$ ($\rho \approx 0°$), while one maximum of B_z is located at $x, y \approx r_W/\sqrt{2}$ ($\rho \approx 45°$).

The circular symmetry of E_p can, in principle, be broken by an electrostatic drift wave along the azimuthal direction. They could be generated by the lower-hybrid drift instability [43, 44], which is caused by gradients in the plasma density and in the magnetic field amplitude. A second possibility is the Simon–Hoh instability that develops if a radial electrostatic field and a spatially uniform orthogonal magnetic field are present [45, 46]. The electron $\mathbf{E} \times \mathbf{B}$ drift destabilizes the plasma. The electric field driving the Simon–Hoh instability would be E_p and the orthogonal magnetic field would be B_z. However, the characteristic wavelengths of the waves driven by both instabilities would be much less than that of the modulation of E_p observed in figure 6. The lower hybrid instability destabilizes wavelengths, which are shorter than the characteristic length scale of the magnetic field gradient and the Simon–Hoh instability requires that B_z be uniform over a scale much larger than the wavelength of the unstable wave. Figure 6(b), furthermore, demonstrates that the electron density distribution is still circularly symmetric. The azimuthal oscillation of E_p is thus not correlated with a charge density modulation and it is probably not an electrostatic wave.

We can understand the modulation of E_p if we take into account the in-plane current (J_x, J_y) and electric field (E_x, E_y) that sustain the localized B_z. We neglect the weak B_p in
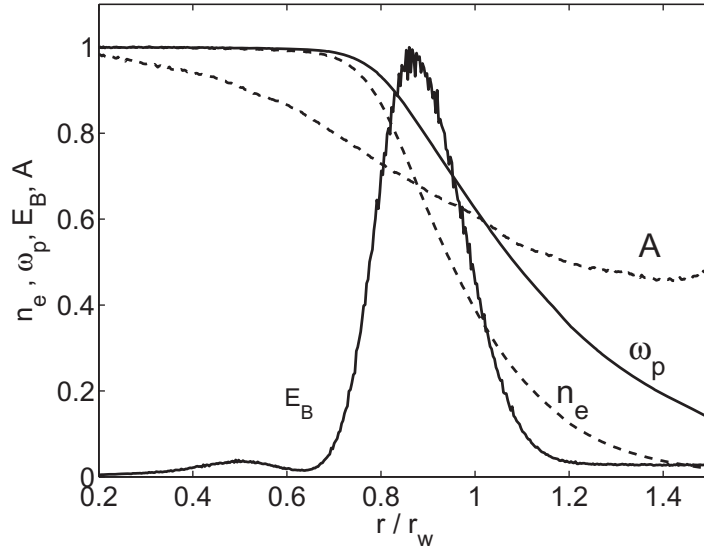
Figure 7. The azimuthally averaged plasma configuration at $t = T_2$: the (dashed) curve n_e corresponds to the radially averaged electron number density $\tilde{n}_e/r$, which is normalized to n_0. The curve ω_p is equal to $(\tilde{n}_e/n_0 r)^{0.5}$ and denotes the local plasma frequency. The curve E_B is the total magnetic energy density $r\langle B_p^2\rangle + r\langle B_z^2\rangle$. The thermal anisotropy $A = K_r(r)/K_\rho(r)$ is the second dashed curve.

figure 5(b). Ampére's law (equation (2)) connects B_z with the in-plane electric field and the in-plane current. Consider the right part of the simulation box $x > 0$ in figure 6(a). The contour lines with $y > 0$ denote a maximum of B_z and those with $y < 0$ a minimum. At $x \approx r_W$ and $y \approx 0$, we find with the right-hand rule that the electric field induced by $\nabla \times (0, 0, B_z)$ gives $\partial_t E_x > 0$ and $\partial_t E_x \gg |\partial_t E_y|$. The electric field amplitude should grow to a sizeable amplitude before a balance between the in-plane current and B_z cancels any further growth of E_p. The superposition of the ambipolar electric field from the rarefaction wave and the practically parallel induced E_x at $x \approx r_W$ and $y \approx 0$ imply that E_p is strong. The induced electric field will also amplify the ambipolar electric field at $x \approx -r_W$ and $y \approx 0$, because both fields reverse their sign. The induced electric field weakens the ambipolar electric field at $x \approx 0$ and $|y| \approx r_W$. A magnetically induced electric field is not tied to charge density modulations, which would explain why the circular symmetry is maintained for the electron density in figure 6(b).

We turn now to the identification of the source mechanism of the magnetic B_z component in figure 5(c). Figure 7 compares the azimuthally averaged energy density $r(\langle B_p^2\rangle + \langle B_z^2\rangle)$ of the magnetic field, the thermal anisotropy $A(r) = K_r(r)/K_\rho(r)$ and the azimuthally averaged electron number density $\tilde{n}_e/r$. The division of $\tilde{n}_e$ by r ensures that a uniform density within the cloud results in a constant value of $\tilde{n}_e/r$ and the multiplication of the azimuthally averaged energy density by r gives us a curve that is proportional to the magnetic energy. These quantities are computed at time T_2.

The onset of the rarefaction wave is found at $r \approx 0.6 r_W$ in figure 7, where the electron density and plasma frequency start decreasing. A sidelobe of the magnetic energy E_B is found within this radius, but most energy is concentrated within $0.7 < r/r_W < 1.1$. The thermal anisotropy curve is a steadily decreasing function up to $r \approx 1.4 r_W$ and is below 1 everywhere.
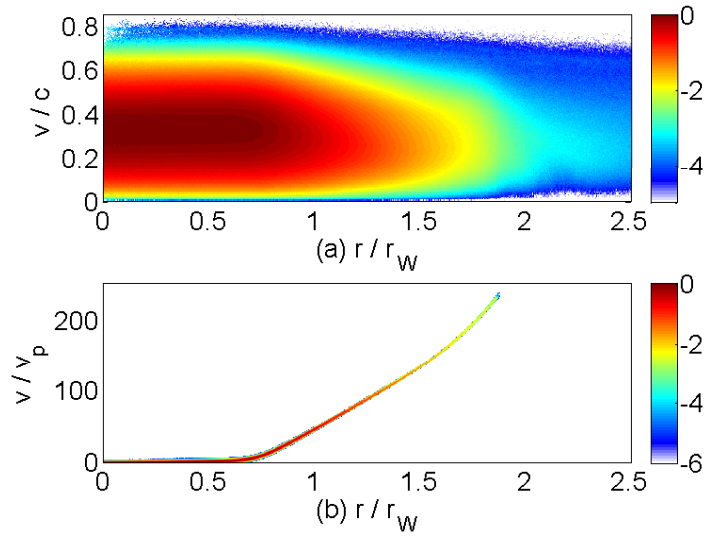
Figure 8. The azimuthally averaged radial phase space density at time T_3 normalized to its initial value: (a) and (b) $\tilde{f}_e$ and $\tilde{f}_p$, respectively. The color scale is 10-logarithmic and r_W is the initial cloud radius.

The mean kinetic energy of the electrons in the radial direction is thus lower than their azimuthal one, which we attribute to the radial proton acceleration. The TAWI destabilizes waves with wave vectors along the cool direction. Figure 5(c) shows that B_z oscillates fastest in the radial direction. One oscillation is visible with the wavelength $\approx 0.8 r_W$. The magnetic B_z component performs two oscillations in the azimuthal direction, each with a wavelength $\approx \pi r_W$. A long oscillation orthogonal to the density gradient has also been observed in simulations of a planar rarefaction wave [32], which is probably a consequence of the density gradient that has not been taken into account by the existing analytic studies.

The simulation data suggest that the large anisotropy observed in figure 7 triggers the TAWI. The E_B peaks at $r \approx 0.85 r_W$, where $A = 0.7$. One may think that E_B should peak in the interval where A is lowest. However, both the growth rate of the TAWI in units of s^{-1} and the magnetic field amplitude the plasma can support an increase with ω_p. The latter can be concluded from the fact that we can normalize the Vlasov–Maxwell set of equations with the help of ω_p. A higher ω_p results in a higher **B** for the same plasma configuration. The magnetic amplitude decreases to noise levels at about $r/r_W \approx 1.5$. It is thus confined to within the rarefaction wave and does not extend into the surrounding electron plasma at this time.

3.3. Final time T3: secondary instability

The electrons have spread out in significant numbers up to $r \approx 2 r_W$ at the time T_3. The radial electric field has accelerated the protons to about $260 v_p$ or 2.6% of c at the time T_3, as we can see from figure 8(b). The protons form a cool beam with one well-defined mean speed for any $r \leqslant 1.8 r_W$. This compact distribution justifies its approximation by a single cold fluid [34]. The mean speed of the protons increases linearly within $0.7 < r/r_W < 1.6$.

Figure 9 shows E_p, B_p and $|B_z|$ at time T_3. The in-plane electric field has weakened, while the magnetic fields have grown further. The plasma density gradient and the ambipolar electric
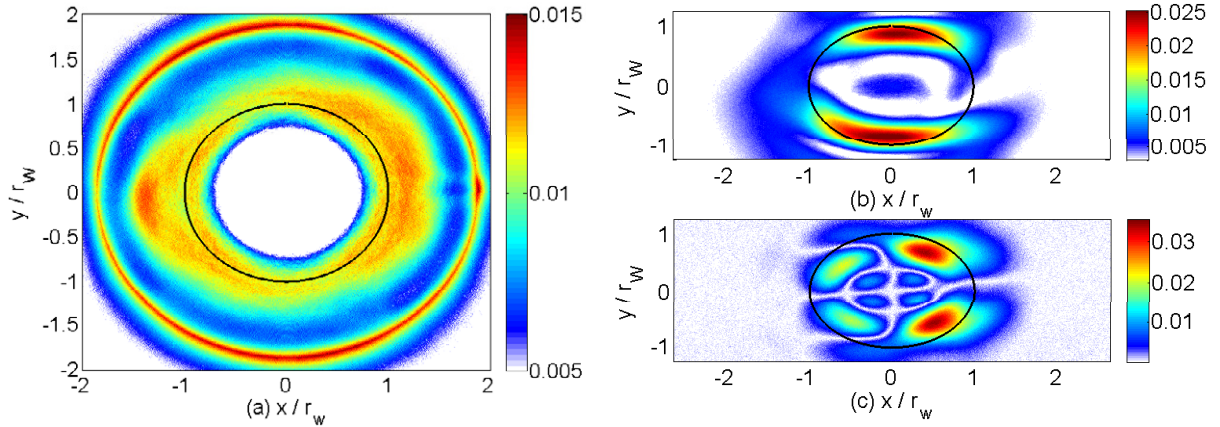
Figure 9. The field distributions at $t = T_3$: (a) the in-plane electric field E_p and (b) the in-plane magnetic field B_p. (c) The modulus $|B_z|$. The black circles with radius r_W outline the initial cloud perimeter.

field in a rarefaction wave decrease with time. The influence on the particle dynamics of the magnetic field and its induced electric field thus become more important. The circular symmetry of E_p imposed by the rarefaction wave is no longer dominant in figure 9(a). The amplitude of the in-plane B_p in figure 9(b) has increased by an order of magnitude compared to that in figure 5(b) and is now comparable to the amplitude of B_z. The distribution of $|B_z|$ in figure 9(c) no longer shows four almost equally important peaks as it did in figure 5(c).

We would expect such a pattern if the wave responsible for the B_p is driven by a separate secondary instability and if it results in a circularly or elliptically polarized magnetowave. An instability is discussed in the next subsection that can generate such a wave. The B_p field oscillates much faster in the radial than in the azimuthal direction in figure 9(b) and its wave vector is thus practically aligned with the radius vector. We call this magnetowave *wave 2*. An elliptically polarized wave will have a B_z component that is phase shifted along r with respect to its B_p component. The B_z component of wave 2 would interfere with the B_z component of the wave that is driven by the TAWI (wave 1). Wave 2 performs one oscillation in the azimuthal direction according to figure 9 and we may assume that the same is true for its B_z component. The B_z field of wave 1 oscillates twice along ρ. So we expect that wave 2 interferes constructively with two half-oscillations of wave 1 and that it interferes destructively with the other two. Interference between both waves could thus explain the pattern observed in figure 9(b).

3.4. Time evolution

Figure 7 has demonstrated that the magnetic field energy density is increased in the radial interval, in which we find a strong thermal anisotropy in the electron distribution. The anisotropy is caused by the loss of electron thermal energy to the radially accelerating protons. Supplementary movie 1 (available from stacks.iop.org/NJP/14/023007/mmedia) animates in time this energy exchange. It shows the electron phase space distribution in (a) and the proton phase space distribution in (b), which are displayed in the form of snapshots and discussed in figures 3, 4 and 8. Movie 1 confirms that electrons, which cross the boundaries on one
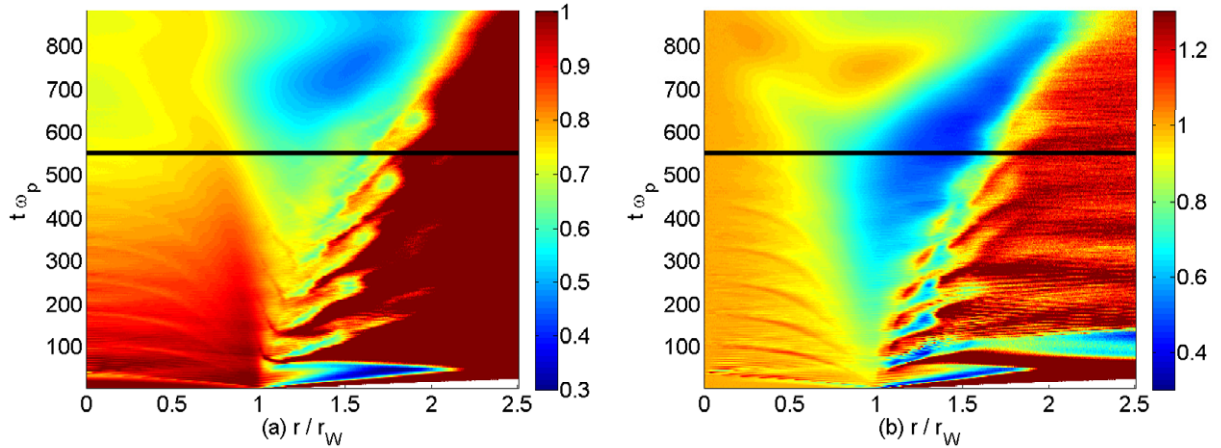
Figure 10. (a) The time evolution of the electron thermal energy $n_0(K_r(r) + K_\rho(r))/2K_0\tilde{n}_e$ and (b) the thermal anisotropy $A(r) = K_r(r)/K_\rho(r)$. The colour scale is linear. The horizontal black line corresponds to time T_2.

side, re-enter on the opposite side, as we expect from the periodic boundary conditions of the simulation. The fastest electrons that escaped from the plasma cloud reach the boundaries at $t \approx 50$ and encounter the electrons that crossed the boundary from the other direction. Note that movie 1(a) shows the velocity modulus and does thus not reveal that both electron populations move into opposite directions. The electron two-stream configuration can result in instabilities. However, the two-stream configuration is rapidly destroyed by the arrival of slower electrons at the boundaries.

Supplementary movie 2 (available from stacks.iop.org/NJP/14/023007/mmedia) demonstrates that the lifetime of the two-stream configuration is too short and the electron density too low to drive detectable instabilities at $t \approx 50$. It animates in time the 10-logarithmic electron density in the simulation box, which is averaged over blocks of 4×4 cells and given in particles per cell. An average density of less than one CP per cell is found close to the boundaries. The local plasma frequency is $\approx \omega_p/100$, which implies a low growth rate for any beam instability [16, 17]. Movie 2 reveals faint electron structures at a time $t \approx 200$ that flow parallel to the x- and y-axis. They are probably caused by an instability between the electrons of the plasma cloud and the electrons that return from the boundary and are accelerated by the ambipolar electric field when they re-enter the cloud [47].

Figure 10 quantifies the energy loss of the electrons to the accelerating protons and also follows the thermal anisotropy in time. Figure 10(a) is a measure of the average kinetic energy per electron, which corresponds to their velocity in the simulation plane. This energy is obtained by summing $K_r(r)$ and $K_\rho(r)$ and by dividing the result by $2K_0\tilde{n}_e/n_0$. K_0 is the initial thermal energy contributed by each velocity component and the division by $\tilde{n}_e/n_0$ gives us a measure of the kinetic energy per electron. The thermal anisotropy $A(r, t)$ is displayed in figure 10(b).

The electrons within the cloud lose about 30% of their kinetic energy to the accelerating protons. The electron kinetic energy is apparently increased outside of the rarefaction wave. This is a selection process, which can be seen in movie 1. The bulk of the slow electrons are contained by the rarefaction wave, while most energetic electrons, which have a kinetic energy that far exceeds the potential energy of the rarefaction wave, can escape.
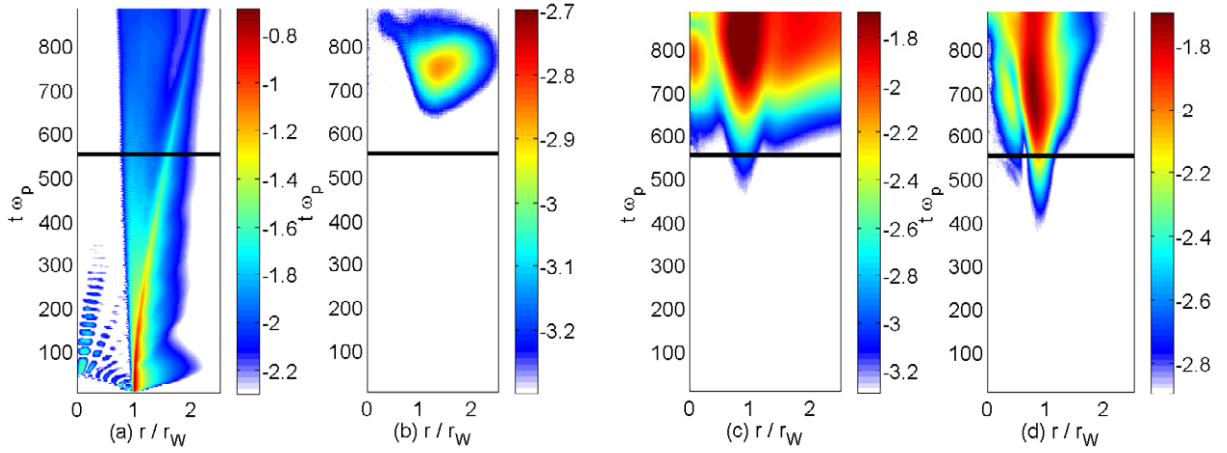
Figure 11. The azimuthally averaged electromagnetic fields $\langle E_p^2 \rangle^{0.5}$ (a), $\langle E_z^2 \rangle^{0.5}$ (b), $\langle B_p^2 \rangle^{0.5}$ (c) and $\langle B_z^2 \rangle^{0.5}$ (d). The color scale is 10-logarithmic. The black horizontal line corresponds to time T_2.

The thermal anisotropy is negligible for the radial interval without a plasma density gradient, e.g. for $r < 0.5 r_W$ and $t = T_2$. $A(r)$ reveals that the electrons in the interval with the proton density gradient lose more energy in the radial than in the azimuthal direction. The radial electron energy is less than half of the azimuthal energy over an extended radial interval. The interval with a value of $A(r) < 0.6$ is largest at time T_2 in figure 10(b), when it covers $0.9 < r/r_W < 1.3$. The B_z saturates at around this time. The TAWI starts to grow at $t \approx 200$, when the anisotropy is sufficiently strong.

The saturation is demonstrated by figure 11, which compares the time evolution of the mean amplitude of the azimuthally averaged fields $\langle E_p^2 \rangle^{0.5}$, $\langle E_z^2 \rangle^{0.5}$, $\langle B_p^2 \rangle^{0.5}$ and $\langle B_z^2 \rangle^{0.5}$. Supplementary movie 3 (available from stacks.iop.org/NJP/14/023007/mmedia) animates in time the spatial distributions of the in-plane electric field E_p (a), the in-plane magnetic field B_p (b) and the B_z. The in-plane electric field E_p in figure 11(a) peaks initially at $r = r_W$. The build-up of this electrostatic field launches electrostatic waves into the cloud, which yields the amplitude peaks for $r < r_W$. The electric field that expands to larger $r > r_W$ and reaches $r \approx 2 r_W$ at $t = 50$ is induced by the electrons that escape from the cloud, e.g. those with $r > r_W$ in figure 3(a). The electron current is not balanced by an ionic current and a radial electric field grows. The density of the escaped electrons decreases as they spread over the simulation box and the electric amplitude eventually drops below the threshold of figure 11(a). The position associated with the maximum of E_p accelerates in time. This maximum coincides with the tip of the rarefaction wave. The electric field with the uniform amplitude of 10^{-2} behind the tip of the ion front roughly outlines the extent of the rarefaction wave. It expands to lower $r < r_W$ as the cloud is progressively eroded. The electric field component E_z in figure 11(b) remains at noise levels, except for a peak at $t \approx T_2$. This peak coincides spatially and temporally with the growth of the rotational magnetowave, which is responsible for the $B_p \neq 0$ in figure 11(c). It is related to the displacement current dE_z/dt connected to B_p.

A comparison of figures 11 (c) and (d) confirms the observation from supplementary movie 3 that B_z starts to grow to a large amplitude well before B_p. The latter grows fastest at around time $t \approx T_2$, when B_z saturates. The presence of a strong B_z is apparently necessary for the

growth of B_p, which supports our previous claim that B_p is driven by a secondary instability. Figure 11 reveals that B_z is confined to within the rarefaction wave, while the magnetic field distribution B_p reaches out into the dilute electron plasma outside of the rarefaction wave. It eventually reaches the boundaries and effects due to the periodic boundary conditions can no longer be neglected at the final time T_F. The development of the strong magnetic fields at $r \approx r_W$ coincide with a balancing of K_r and K_ρ in figure 10(b). This change in A is partially due to the electron deflection by **B**, which will contribute to an equilibration of K_r and K_ρ.

We want to determine the source mechanism of the in-plane magnetic field B_p. The ambipolar electric field due to the rarefaction wave and the electric field induced by B_z are both confined to the simulation plane. The electric fields and B_z can exert a force on the electrons only in this plane and no current orthogonal to the simulation plane can be generated. Since we have no initial beams moving along the z-axis, we can rule out magnetic beam instabilities [16, 17, 24]. One possibility to generate an electron flow along z is a coupling of the electron velocity components through the Lorentz factor. An electron acceleration in the simulation plane would change v_z. The fastest electrons in figure 4(a) have the mildly relativistic speed $v \approx 0.7c$ that gives a Lorentz factor $\Gamma \approx 1.4$. However, their number density is low and we could not expect them to drive strong in-plane magnetic fields. A possible mechanism for the growth of B_p is the electric field induced by B_z. The induced field is strong when B_z saturates and it changes the direction of the in-plane electric field vector by up to 5% relative to the radius vector. The plasma density is according to figure 6(b) circularly symmetric at $t = T_2$. A misalignment of the in-plane electric field vector and the density gradient can give rise to elliptically polarized magnetowaves [39, 40].

4. Discussion

We have examined here the expansion of an initially unmagnetized circular plasma cloud into a vacuum by means of a 2D3V PIC simulation. The purpose of our study has been to test whether a TAWI can also develop in curved rarefaction waves. Previous studies considered planar plasma slabs that expanded under their own thermal pressure [32] and observed the growth of strong magnetic fields in the rarefaction wave, unless a shock suppressed the TAWI [37, 38].

A thermally anisotropic electron distribution develops due to two reasons. Firstly, the slowdown of the electrons in the ambipolar electric field implies that their thermal pressure is decreased along the density gradient. This mechanism occurs in planar and curved rarefaction waves. Secondly, the inelastic reflection of an electron by the expanding rarefaction wave implies that it loses momentum along the electric field direction. This momentum is transferred to the accelerating ions. The initial plasma distribution used in [32, 37, 38] is a plasma slab of infinite extent in one direction, which has a finite width in the second direction. This plasma slab is immersed in a vacuum or in a low-density plasma. Both plasma boundaries are parallel. This implies that every reflection of the electron will decrease the same momentum component, namely the component that is aligned with the antiparallel density gradients of both rarefaction waves. The anisotropy increases with every electron reflection. This mechanism cannot occur in a circular rarefaction wave, since here consecutive electron reflections tend to decrease different momentum components. Our study can thus test whether consecutive electron reflections are necessary to achieve a TAWI.

If the slowdown of the electrons in the ambipolar electric field of a plasma with a spatially non-uniform density is enough to trigger the TAWI, then this instability may play a role in the

magnetization of astrophysical plasma [31] besides the filamentation instability [9] and cosmic ray-driven instabilities [8]. The magnetic energy that can be generated by the TAWI is a fraction of the electron thermal energy, here about 1%. This energy density is well below that of the filamentation instability, which can reach about 10–20% of the kinetic energy density of leptonic beams if they are cold. However, the TAWI requires only hot electrons and a density gradient to grow, while the filamentation instability is triggered by relativistic particle beams that we may find only close to plasma shocks. The TAWI could thus magnetize much larger intervals in energetic astrophysical jets, such as GRB jets, which are thought to have a nonuniform plasma density and relativistically hot electrons. The TAWI may also generate a seed magnetic field in the turbulent plasma close to SNR shocks and speed up the development of the much more powerful cosmic ray-driven instabilities.

Our findings are as follows. The electron expansion results in a strong radial electrostatic field. It counteracts a further electron expansion and accelerates the protons into the radial direction. A rarefaction wave emerges, which is characterized by an increase of the proton mean speed and by a decrease of the proton density with an increasing radius. The expansion of a rarefaction wave is self-similar [33–35]. The absence of an ambient medium has prevented the formation of a shock and the protons could reach a speed exceeding 250 times their thermal speed.

The fields within the rarefaction wave were initially electrostatic. Electrons lose momentum to the accelerating protons only in the radial direction, which implies that their radial thermal pressure decreases more quickly than the azimuthal one. A TAWI [19] grows once the radial extent of the rarefaction wave is sufficient to accommodate a wavelength of the unstable modes [32] and once the thermal anisotropy between the radial and the azimuthal direction become sufficiently large. The TAWI results in the aperiodic growth of a TM wave. This TM wave induces an electric field that is added to that of the electrostatic ambipolar electric field of the rarefaction wave. The total electric field is thus no longer parallel to the plasma density gradient.

A misalignment between the electric field and the plasma density gradient can drive circularly or elliptically polarized magnetowaves [39, 40]. We propose that these waves are responsible for the in-plane magnetic field we observe in our simulation, which cannot be explained in terms of the TAWI. The magnetic fields of this wave reach an amplitude that is comparable to the waves due to the TAWI.

Our findings can be verified in an experiment where the absorption of a laser pulse heats up the electrons in a thin wire [48]. Some electrons will leave the now positively charged wire and build up an ambipolar electric field. This ambipolar field accelerates the ions through the transverse normal sheath acceleration (TNSA) mechanism [49, 50] and it results in the formation of a rarefaction wave. The ablation of a wire generates a cylindrical rarefaction wave. Our circular plasma cloud corresponds to an idealized cross section of the wire, as long as it is sufficiently far away from the laser impact point [48]. The cross section is idealized, because we do not consider ionization processes that require more elaborate numerical codes [51, 52]. The plasma dynamics outside of the wire should be comparable in the simulation and experiment. The strong magnetic fields that develop in the rarefaction wave should be detectable. It is thus possible to investigate systematically the TAWI in a controlled laboratory experiment and to determine the strength and lifetime of the magnetic field. The interplay of the TAWI with the secondary magnetowave we have observed here and other instabilities, such as the Rayleigh–Taylor instability [53, 54], can also be examined.

IOP Institute of Physics ⬦ DEUTSCHE PHYSIKALISCHE GESELLSCHAFT

The experiment can reveal the topology of the magnetic fields in a three-dimensional setting, which is currently computationally too expensive.

References

[1] Aharonian F A *et al* 2004 *Nature* **432** 75
[2] Fender R and Belloni T 2004 *Ann. Rev. Astron. Astrophys.* **42** 317
[3] Piran T 2004 *Rev. Mod. Phys.* **76** 1143
[4] Medvedev M V 2000 *Astrophys. J.* **540** 704
[5] Bykov A M and Treumann R A 2011 *Astron. Astrophys. Rev.* **19** 42
[6] Blandford R D and Eichler D 1987 *Phys. Rep.* **154** 1
[7] Berezhko E G, Ksenofontov L T and Volk H J 2003 *Astron. Astrophys.* **412** L11
[8] Bell A R 2004 *Mon. Not. R. Astron. Soc.* **353** 550
[9] Medvedev M V and Loeb A 1999 *Astrophys. J.* **526** 697
[10] Brainerd J J 2000 *Astrophys. J.* **538** 628
[11] Gruzinov A 2001 *Astrophys. J.* **563** L15
[12] Waxman E 2006 *Plasma Phys. Control. Fusion* **48** B137
[13] Kazimura Y, Sakai J I, Neubert T and Bulanov S V 1998 *Astrophys. J.* **498** L183
[14] Silva L O, Fonseca R A, Tonge J W, Dawson J M, Mori W B and Medvedev M V 2003 *Astrophys. J.* **596** L121
[15] Schlickeiser R and Shukla P K 2003 *Astrophys. J.* **599** L57
[16] Bret A, Gremillet L and Dieckmann M E 2010 *Phys. Plasmas* **17** 120501
[17] Bret A, Firpo M C and Deutsch C 2005 *Phys. Rev. Lett.* **94** 115002
[18] Kapetanakos C A 1974 *Appl. Phys. Lett.* **25** 484
[19] Weibel E S 1959 *Phys. Rev. Lett.* **2** 83
[20] Kalman B G, Montes C and Quemada D 1968 *Phys. Fluids* **11** 1797
[21] Morse R L and Nielson C W 1971 *Phys. Fluids* **14** 830
[22] Davidson R C, Hammer D A, Haber I and Wagner C E 1972 *Phys. Fluids* **15** 317
[23] Kaang H H, Ryu C M and Yoon P H 2009 *Phys. Plasmas* **16** 082103
[24] Bret A 2007 *Contrib. Plasma Phys.* **47** 133
[25] Stockem A, Dieckmann M E and Schlickeiser R 2009 *Plasma Phys. Control. Fusion* **51** 075014
[26] Stockem A, Dieckmann M E and Schlickeiser R 2010 *Plasma Phys. Control. Fusion* **52** 085009
[27] Palodhi L, Califano F and Pegoraro F 2009 *Plasma Phys. Control. Fusion* **51** 125006
[28] Lazar M, Schlickeiser R and Poedts S 2010 *Phys. Plasmas* **17** 062112
[29] Tautz R C 2011 *Phys. Plasmas* **18** 012101
[30] Shaisultanov R and Eichler D 2011 *Phys. Plasmas* **18** 034501
[31] Schlickeiser R 2005 *Plasma Phys. Control. Fusion* **47** A205
[32] Thaury C, Mora P, Heron A and Adam J C 2010 *Phys. Rev.* E **82** 016408
[33] Sack C and Schamel H 1987 *Phys. Rep.* **156** 311
[34] Grismayer T, Mora P, Adam J C and Heron A 2008 *Phys. Rev.* E **77** 066407
[35] Lyutikov M 2010 *Phys. Rev.* E **82** 056305

[36] Gargate L, Fonseca R A, Bingham R and Silva L O 2008 *IEEE Trans. Plasma Sci.* **36** 1168
[37] Sarri G, Dieckmann M E, Kourakis I and Borghesi M 2011 *Phys. Rev. Lett.* **107** 025003
[38] Sarri G, Murphy G C, Dieckmann M E, Bret A, Quinn K, Kourakis I, Borghesi M, Drury L O C and Ynnerman A 2011 *New J. Phys.* **13** 073023
[39] Saleem H 1996 *Phys. Rev.* E **54** 4469
[40] Saleem H 2009 *Phys. Plasmas* **16** 082102
[41] Eastwood J W 1991 *Comput. Phys. Commun.* **64** 252
[42] Dawson J M 1983 *Rev. Mod. Phys.* **55** 403
[43] Daughton W, Lapenta G and Ricci P 2004 *Phys. Rev. Lett.* **93** 105004
[44] Lapenta G and Brackbill J U 2002 *Phys. Plasmas* **9** 1544
[45] Simon A 1963 *Phys. Fluids* **6** 382
[46] Sakawa Y, Joshi C, Kaw P K, Jain V K, Johnston T W, Chen F F and Dawson J M 1992 *Phys. Rev. Lett.* **69** 85
[47] Dieckmann M E, Sarri G, Romagnani L, Kourakis I and Borghesi M 2010 *Plasma Phys. Control. Fusion* **52** 025001
[48] Quinn K *et al* 2009 *Phys. Rev. Lett.* **102** 194801
[49] Snavely R A *et al* 2000 *Phys. Rev. Lett.* **85** 2945
[50] d'Humieres E, Lefebvre E, Gremillet L and Malka V 2005 *Phys. Plasmas* **12** 062704
[51] Gibbon P, Beg F N, Clark E L, Evans R G and Zepf M 2004 *Phys. Plasmas* **11** 4032
[52] Nuter R, Gremillet L, Lefebvre E, Levy A, Ceccotti T and Martin P 2011 *Phys. Plasmas* **18** 033107
[53] Piriz A R, Di Lucchio L and Prieto G R 2011 *Phys. Plasmas* **18** 012702
[54] Piriz A R, Sanz J and Ibanez L F 1997 *Phys. Plasmas* **4** 1117